Catalysis Today 470 (2026) 115764

Contents lists available at ScienceDirect

Catalysis Today

journal homepage: www.elsevier.com/locate/cattod

α-FeOOH-Intercalated $Ti_3C_2T_x$ MXene as a new and stable heterogeneous Fenton catalyst for caffeine degradation in water

Shalu Atri [a,*], Hamidreza Behtooei [a], Mario Kotlar [b], Frantisek Zazimal [c], Dana Dvoranova [d], Tomas Roch [e], Leonid Satrapinskyy [e], Tomas Zelenka [f], Tomas Homola [c], Olivier Monfort [a,*]

[a] Department of Inorganic Chemistry, Faculty of Natural Sciences, Comenius, University Bratislava, Ilkovicova 6, Mlynska dolina, Bratislava 842 15, Slovakia
[b] Center for Nanodiagnostics of Materials, Faculty of Materials Science and Technologyin Trnava, Slovak University of Technology in Bratislava, Slovakia, Vazovova 5, Bratslava 812 43, Slovakia
[c] Department of Plasma Physics and Technology, Faculty of Science Masaryk University , Masaryk University, Brno 611 37, Czechia
[d] Institute of Physical Chemistry and Chemical Physics, Faculty of Chemical and Food Technology, Slovak University of Technology in Bratislava, Radlinskeho 9, Bratislava 81237, Slovakia
[e] Centre for Nanotechnology and Advanced Materials, Faculty of Mathematics, Physics and Informatics, Comenius University Bratislava, Mlynska dolina, Bratislava 842 48, Slovakia
[f] Department of Chemistry, Faculty of Science, University of Ostrava, 30. dubna 22, Ostrava 702 00, Czechia

ARTICLE INFO

Keywords:
MXene
Hybrid MXene/Fenton catalyst
Stabile Fenton
Wastewaters treatment
Peroxymonosulfate activation

ABSTRACT

This study demonstrates a simple and scalable synthesis of α-FeOOH (goethite) intercalated $Ti_3C_2T_x$ MXene through TMAOH treatment, targeting efficient degradation of emerging micropollutants in wastewater via an advanced oxidation process (AOP). Such a α-FeOOH-intercalated MXene stabilizes heterogeneous Fenton-based reactions which usually suffer from decreased efficiency over time due to Fe leaching, thus highlighting the novelty of the work. The successful integration of goethite particles in the MXene interlayer space was evidenced by X-ray diffraction (XRD), Fourier-transform infrared spectrometer (FTIR) and Transmission Electron Microscopy (TEM) analysis. X-ray photoelectron analysis (XPS) revealed notable surface oxidation along with minor TiF_x and $TiO_{2-x}F_x$ impurities formed via TMAOH treatment. Increased concentration of surface functional groups along with enhanced BET area (71.2 $m^2\ g^{-1}$) and porosity after TMAOH treatment enabled complete degradation of caffeine in ~ 90 min, by activation of peroxymonosulfate (PMS) under UVA light. Scavenging experiments, electron paramagnetic resonance (EPR) and XPS analysis indicated the degradation mechanism driven by Fenton-based reactions, electron transfer and interfacial surface charge transfers, with hydroxyl ($^{\bullet}OH$) and sulfate ($SO_4^{\bullet-}$) radicals identified as predominant reactive oxygen species (ROS). The assessment of the α-FeOOH-intercalated MXene as stable Fenton catalyst was confirmed with minimal iron leaching (3.07 wt%) during catalytic reactions and robust reusability over ten cycles, thus being more efficient and sustainable than conventional Fenton-based catalysts. Post-reaction XRD,FTIR and TEM analyses further confirmed excellent structural stability of the new catalyst. These findings establish α-FeOOH-intercalated $Ti_3C_2T_x$ MXene as a promising and durable catalyst for heterogeneous Fenton-based reactions applied to wastewaters treatment.

1. Introduction

Removing micropollutants (MPs) from surface water is a major environmental challenge [1]. Caffeine (CAF) is classified as pharmaceutical active compound (PhAC) and it is widely used in the pharmaceutical industry. CAF commonly enters aquatic systems through effluents from wastewater treatment plants (WWTPs) [2]. While its presence originates from human consumption (e.g. beverages and pharmaceuticals), the primary reason for its occurrence in surface water is the inefficiency of WWTPs in completely removing CAF [3]. In Europe, CAF concentration in freshwater can reach up to 3500 ng L^{-1} near WWTP [4]. In marine environment, the concentrations range from 4.5 to 1110 ng L^{-1} in the Atlantic Ocean and Adriatic Sea, whereas lower levels are exhibited in the Baltic Sea (0.016–0.058 ng L^{-1}) [5,6]. Therefore, CAF can be considered as widespread aquatic contaminant with environmental risks due to its persistence and toxicity to aquatic

* Corresponding authors.
E-mail addresses: shalu1@uniba.sk (S. Atri), olivier.monfort@uniba.sk (O. Monfort).

https://doi.org/10.1016/j.cattod.2026.115764
Received 15 November 2025; Received in revised form 11 February 2026; Accepted 5 March 2026
Available online 14 March 2026

organisms [7]. Moreover, in 2024, the European Commission adopted a new directive on urban wastewater treatment (Directive No. 2024/3019), which applies from January 2025 [8]. This directive mandates stricter regulations to reduce pharmaceutical MPs by requiring, for instance, the implementation of quaternary treatment processes and achieving a minimum removal efficiency of **80%** for selected MPs [8]. Thus, the need of innovative technologies to implement into WWTP allowing for MPs removal is one of the biggest challenges for the protection of the water resource.

Among the promising quaternary treatment strategies, advanced oxidation processes (AOPs) have been identified as potential technology since they allow mineralization of MPs into harmless products like H_2O and CO_2 [9]. Sulfate radical-based AOPs (SR-AOPs) show great promise due to high oxidation potential of sulfate radicals ($SO_4^{\bullet-}$; $E^0 = 2.5–3.1V$), along with their longer lifetime and wide pH stability from acidic to near neutral compared to hydroxyl radicals ($^{\bullet}OH$) [10]. To activate SR-AOPs, binary metal oxides, especially those based on iron, are widely investigated as Fenton-based catalysts, but one of their main drawbacks is their instability associated with metal leaching [11]. Although they can generate $^{\bullet}OH$ and $SO_4^{\bullet-}$, Fenton-based catalysts suffer from the poor stability of Fe(III)/Fe(II) redox cycle, especially in iron oxides/oxo-hydroxides like hematite (α-Fe_2O_3), magnetite (Fe_3O_4) or goethite(α-FeOOH), thus highlighting the importance of finding innovation for the stability of such catalysts [12]. One challenge is based on the design of innovative support for heterogeneous Fenton catalysts that tackle out the above-mentioned drawbacks and that improve surface area, electron transfer and reaction kinetics [13]. MXenes, which are referred as two-dimensional (2D) transition metal carbides/nitrides or carbonitrides [14], represented by the formula $M_{n+1}X_nT_z$ (M = early transition metal, X = C, N, T_z = functional groups such as -OH, -F, and -O) can play the role of innovative support for iron oxides/oxo-hydroxides.

In our work, we consider $Ti_3C_2T_x$ MXene as support to construct a hybrid catalyst [15], as it exhibits abundant surface terminations that facilitate intercalation, electron transfer and structural stability for host material [16]. To expand the MXene interlayer spacing and increase its surface area, tetramethyl ammonium hydroxide (TMAOH) has been reported as an effective reagent for delaminating multilayer $Ti_3C_2T_x$ into few-layer nanosheets [17]. Using this strategy, we explore the possibility of intercalating α-FeOOH within the MXene structure, as goethite is a widely used Fenton catalyst with low cost and high surface area but strongly limited by iron leaching [18,19]. Our aim is to develop an efficient and stable Fenton-based catalyst by combining goethite with MXene's unique properties. Herein, we report a facile, scalable and low-temperature synthesis of α-FeOOH-intercalated $Ti_3C_2T_x$ MXene through TMAOH treatment. This approach uniquely harnesses α-FeOOH stabilization in MXene interlayer space to overcome limitations linked to the instability of heterogeneous Fenton-based processes, thus highlighting a new advancement in MXene-based catalytic systems for quaternary wastewaters treatment. Accordingly, the key novelty of this work lies in the stabilization of Fenton catalytic sites through MXene interlayer confinement via formation of a new hybrid MXene/Fenton catalyst, enabling an efficient and durable heterogeneous Fenton process.

2. Experimental section

2.1. Preparation of α-FeOOH-intercalated $Ti_3C_2T_x$ (FTTOH)

To prepare the Fe intercalated $Ti_3C_2T_x$ powder (FTTOH), iron(III) nitrate nonahydrate ($Fe(NO_3)_3.9H_2O$; ACS reagent, ≥ **98%**), with Fe content from 0.69 wt% to 8.52 wt% (relative to $Ti_3C_2T_x$), was added *in situ* to a mixture of 0.5 g of $Ti_3C_2T_x$ dispersed in 2.5 mL TMAOH and 2.5 mL deionized water (DI) after 20 h of stirring. The mixture was then stirred for an additional 3 h at 25 °C. The product was collected using centrifugation at 4500 rpm for 15 min (per cycle), washed with DI water until neutral pH was achieved, and subsequently dried at 80 °C for 2 h.

For the control samples, α-FeOOH was synthesized by using the same procedure, excluding the addition of MXene. The control $Ti_3C_2T_x$ powder (TTOH) treated by TMAOH (Thermo scientific, 1.0 M aq. Soln., ACS reagent) was prepared using 0.5 g of $Ti_3C_2T_x$ powder which dispersed in a mixture of 2.5 mL TMAOH and 2.5 mL DI water. The suspension was stirred at room temperature for 20 h. The resulting product was washed repeatedly with DI water until neutral pH, and collected using centrifugation at 4500 rpm for 15 min per cycle. The final product was dried at 80 °C for 2 h. It is worth noting multilayer $Ti_3C_2T_x$ MXene which was used during the synthesis was prepared using 1.0 g of Ti_3AlC_2 MAX phase powder (Sigma-Aldrich, ≥ **90%**), which was gradually added to an etching solution composed of 9 mL of DI water, 18 mL of 12 M hydrochloric acid (HCl; Merck, **37%**) and 3.0 mL of 28.4 M hydrofluoric acid (HF; Thermo Scientific, ACS Reagent, 48-**51%** solution in water) in a plastic bottle, following a previously established procedure [20].

2.2. Characterization techniques

The structural and phase composition of the prepared $Ti_3C_2T_x$, TTOH, FTTOH and α-FeOOH samples were analyzed using a PANalytical X-ray diffractometer (XRD) equipped with Cu Kα radiation (λ = 1.5406 Å), operating over a 2θ range of 3°–80°. The chemical bonds of the MXene-based samples were analyzed using a Fourier-transform infrared spectrometer (FTIR; JASCO 4600) before and after reaction to identify chemical modifications. Morphological characteristics were examined using scanning electron microscopy (SEM; Tescan Lyra III) and transmission electron microscopy (TEM; JEOL JEM ARM 200 cF). The catalysts for TEM were prepared by dispersing the powder in isopropyl alcohol, followed by 5 min of sonication and deposition onto thin, carbon-coated copper grids. Surface chemistry was investigated by X-ray photoelectron spectroscopy (XPS) using an AXIS Supra spectrometer (Kratos Analytical Ltd., UK) equipped with a monochromatic Al Kα X-ray source (photon energy = 1486.6 eV, emission current = 10 mA, acceleration voltage = 15 kV). Charge compensation during XPS analysis was achieved using an automatic electron flood gun. Wide-scan and core-level spectra were acquired at pass energies of 80 eV and 20 eV, respectively. The pressure in the XPS analysis chamber was maintained at approximately 10^{-7} Pa during measurements. XPS spectra of TTOH and FTTOH were referenced to the C 1 s peak at 284.8 eV (C–Ti bonds) [19] leading to position of C-C/C-H signal at 285.0 (FTTOH) and 285.1 eV (TTOH). The spectra of α-FeOOH were referenced using C-C/C-H signal at 285.0. Data were processed and analyzed using Casa XPS software. To subtract the signal of inelastically scattered electrons, Shirley background was employed. Nitrogen adsorption-desorption at 77 K was measured by Sync 400 (3 P Instruments) as described previously [20]. Prior to analysis, the samples were degassed in two steps: 16 h at 423 K in a vacuum oven and 4 h at 413 K in the analyzer. Porous properties were calculated using ASiQwin software (Quantachrome Instruments). The BET area was calculated according to Rouquerol's consistency criteria [21,22]. Micropore (< 2 nm) and mesopore (2–50 nm) volumes were obtained by integrating the pore size distribution (PSD) derived from the adsorption branch using the QSDFT (Quenched Solid Density Functional Theory) model, assuming carbon-like slit micropores and cylindrical mesopores.

2.3. Catalytic degradation of caffeine and related analyses

The degradation of CAF using peroxymonosulfate (PMS) activation *via* the synthesized catalyst under UVA light was performed in a batch mode in home-made box photo-reactor (Foto-Sihor) equipped with 4 UVA lamps (Sylvania BL368–15W with a total irradiance of 1.29 cm^{-2} in the range 335 – 380 nm). For each experiment, a 50 mL solution of 50 μM CAF contained 0.2 L^{-1} of the suspended catalyst and 0.5 mM of PMS (OXONE®, Sigma Aldrich). Prior to the degradation experiment, the suspension without PMS was magnetically stirred in the dark for

10 min to reach adsorption-desorption equilibrium. The reaction was initiated by adding PMS and turning on UVA light (under continuous stirring). At designated time intervals, 500 μL aliquots were withdrawn, immediately filtered through a 0.45 μm PTFE membrane and transferred into a HPLC vial, containing 100 μL methanol (MeOH, CentralChem, Slovakia) as a quenching agent to stop residual reactions.

The experimental conditions were optimized by varying systematically selected parameters, including Fe wt% in the catalyst (0.69, 1.37, 2.93, **8.52%**), catalyst dosage (0.04, 0.1, 0.2, 0.4, 0.8 L^{-1}), PMS concentrations (0.1, 0.2, 0.4, 0.5 and 1.0 mM), and pH (3, 4, 5, 7, 9, 11) as demonstrated in Figure S1 and Text S1. Based on these results, 0.2 L^{-1} of FTTOH catalyst (containing 2.93 wt% Fe), 0.5 mM PMS and the natural pH of the system (pH ~ 4) were selected for the experiments discussed in this work.

Concerning the monitoring of CAF degradation, its concentration was determined using high performance liquid chromatography (HPLC, 1260 Infinity III Agilent), equipped with a C18 column (Hypersil Gold, 5μm 150 mm × 4.6 mm, Thermo Fisher Scientific) and DAD detector (wavelength detection set at 272 nm). The mobile phase was a mixture of HPLC grade methanol (MeOH, Merck) and HPLC grade water (H_2O, Merck) in gradient mode (Table S1), with a flow rate of 1.0 mL min^{-1}.

To identify and determine the contribution of reactive oxygen species (ROS) involved in the CAF degradation *via* PMS activation, scavenging experiments were conducted using various quenchers: 10 mM tert-butanol (TBA, EMSURE® ACS analysis, Merck) for $^{\bullet}OH$, 10 mM isopropanol (ISOP, LiChrosolv®, Merck) for both $^{\bullet}OH$ and $SO_4^{\bullet-}$ and a combination of 10 mM of ISOP and 0.5 mM of furfuryl alcohol (FFA, Analytical standard, Sigma Aldrich) for singlet oxygen ($^1O_2$). The concentration of quenchers was determined based on calculations detailed in the Supplementary Information (Text S2 and Table S2) [23]. In addition, based on the apparent rate constant (k_{app}) obtained during the scavenging experiments, the contribution of the identified ROS can be calculated to provide better insights into the understanding of the CAF degradation in the investigated system (Text S3 and Table S2). Details of the electron paramagnetic resonance (EPR) experimental setup, including irradiation conditions and spectral analysis, are given in the Supporting Information (Text S4).

2.4. Assessment of FTTOH as stable Fenton catalyst

Catalyst reusability was assessed over ten consecutive degradation cycles under identical conditions (50 mL of 50 μM CAF, 0.2 L^{-1} catalyst, 0.5 mM PMS under UVA light). After each cycle, the catalyst was recovered *via* centrifugation, washed thoroughly with deionized water, and dried at 80 °C for reuse. The structural stability of the catalyst was evaluated through XRD, TEM, FTIR and iron-leaching analysis using colorimetric ferrozine method, following the protocol described in the literature [24]. The iron leaching is considered crucial for both structural integrity and assessment of heterogeneous *vs.* homogeneous Fenton reactions. The consumption of PMS during CAF degradation was also monitored using colorimetric KI method, according to the literature [25].

To tackle out the potential contribution of homogeneous Fenton reactions, CAF degradation was performed under optimized conditions for FTTOH system but replacing the catalyst by iron perchlorate ($Fe(ClO_4)_3.xH_2O$; Sigma-Aldrich) at an iron concentration equivalent to leached amount detected for FTTOH system. For comparison purpose, goethite was tested for CAF degradation under similar conditions as the optimized FTTOH system.

3. Results and discussion

3.1. Synthesis of FTTOH and structural characterization

The preparation of FTTOH samples involved a two-step process as shown in Fig. 1. First, multilayer $Ti_3C_2T_x$ MXene was synthesized through mixed acid etching of the corresponding MAX phase. In the second step, the resulting MXene was exfoliated using TMAOH treatment (TTOH), followed by α-FeOOH-intercalation (Fig. 1).

Fig. 2 presents the XRD patterns of synthesized materials including $Ti_3C_2T_x$, MXene, TMAOH modified MXene (TTOH), α-FeOOH and α-FeOOH-intercalated MXene (FTTOH). The $Ti_3C_2T_x$ MXene exhibits a broad (*002*) reflection near 8.3 °, characteristic of well-stacked MXene layers with typical interlayer spacing after etching. Upon treatment with TMAOH, the (*002*) reflection in TTOH becomes sharp and intense with a significant shift to a lower angle of 5.8 °, indicating increased interlayer spacing due to solvent intercalation and partial delamination, alongside slight disruption of layer stacking [26]. The phase identification of synthesized goethite (α-FeOOH) shows good agreement with the ICSD reference pattern (ICSD-01–081–0462) using X'Pert HighScore software (Fig. 2b). This confirms that α-FeOOH crystallizes in an orthorhombic symmetry with space group *Pbnm*, and the observed diffraction peaks at

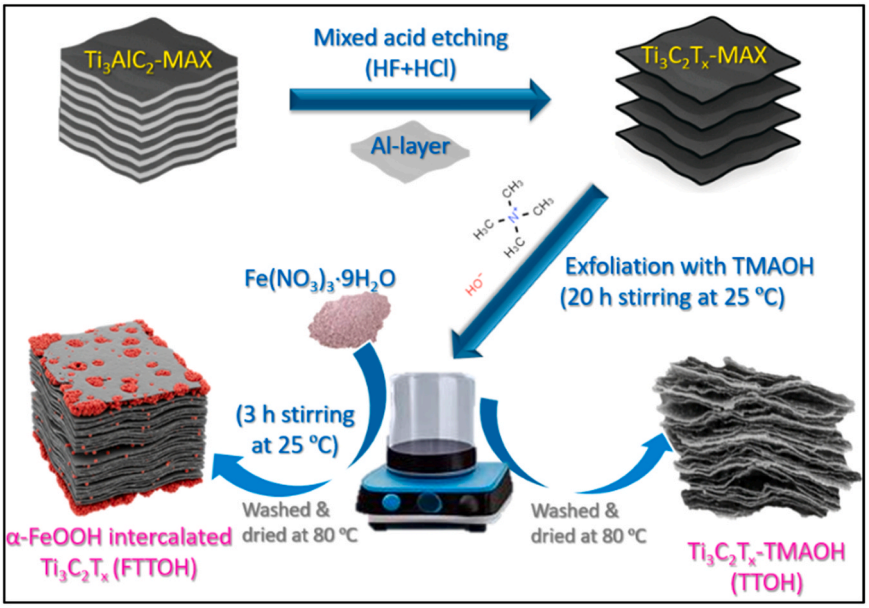

Fig. 1. Schematic representation of the preparation of TTOH and FTTOH.

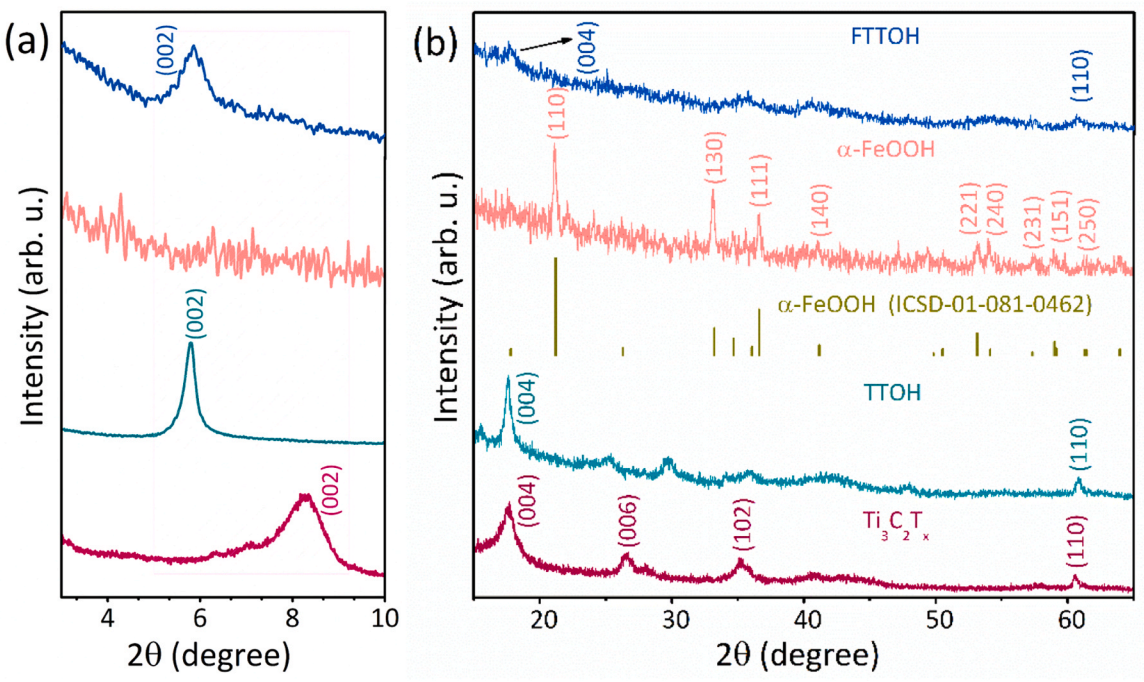

Fig. 2. XRD patterns of acid-etched $Ti_3C_2T_x$, TTOH, α-FeOOH and the corresponding line diagram of α-FeOOH (ICSD-01–081–0462) and FTTOH samples in the range of (a) 3–10° and (b) 15–65°.

(*110*), (*130*), (*111*), (*140*), (*150*), (*221*), (*231*) and (*151*) can be indexed with lattice parameters a = 4.6188 Å, b = 9.9528 Å, c = 3.0236 Å [27].

Upon α-FeOOH intercalation in the FTTOH sample, the (*002*) peak becomes significantly broader and less intense while maintaining a similar position, reflecting increased structural disorder, variable interlayer distances, and lattice distortion induced by α-FeOOH incorporation within the MXene layers (Fig. 2a). In the mid- to high-angle region (15°–65°), all three samples show broad and weak reflections typical of $Ti_3C_2T_x$, corresponding to higher-order basal planes ((*004*) and (*006*) and in-plane lattice planes (Fig. 2b). The absence of distinct α-FeOOH diffraction peaks in the XRD pattern of FTTOH likely arises from its low loading (~ 5 wt%), poor crystallinity and high dispersion within the $Ti_3C_2T_x$ layers, which collectively reduce its diffraction intensity below the detection limit. Compared to the $Ti_3C_2T_x$ and TTOH, the FTTOH sample exhibits a noticeable decrease in peak intensity and increased peak broadening in this region as well, consistent with reduced crystallinity and enhanced structural perturbations caused by α-FeOOH intercalation, confirming the effective modification of the layered structure of $Ti_3C_2T_x$ MXene, that may contribute to improved surface accessibility and catalytic performance.

Fig. 3 displayed the FTIR spectra of both $Ti_3C_2T_x$, TTOH, α-FeOOH and FTTOH samples, from which largely similar vibrational features corresponding to typical chemical bonds forming MXene and intercalated species can be observed (Fig. 3a-b). The characteristic bands associated with O-H stretching (~3430 cm^{-1}), H-O-H bending (~1630 cm^{-1}), C-H bending (~1390 cm^{-1}), C-N stretching (~950 cm^{-1}), and Ti-O bending (~550–650 cm^{-1}) vibrations are present in both samples, being consistent with -OH, -O, -F terminations, intercalated water molecules, and TMAOH-related organic groups [28-30]. The band centred at 1346 cm^{-1} and 619 cm^{-1} corresponds to Fe-O vibrational modes in α-FeOOH [31]. The band observed at 3110 cm^{-1} revealed O-H stretching mode in the goethite structure. The characteristic band appearing at

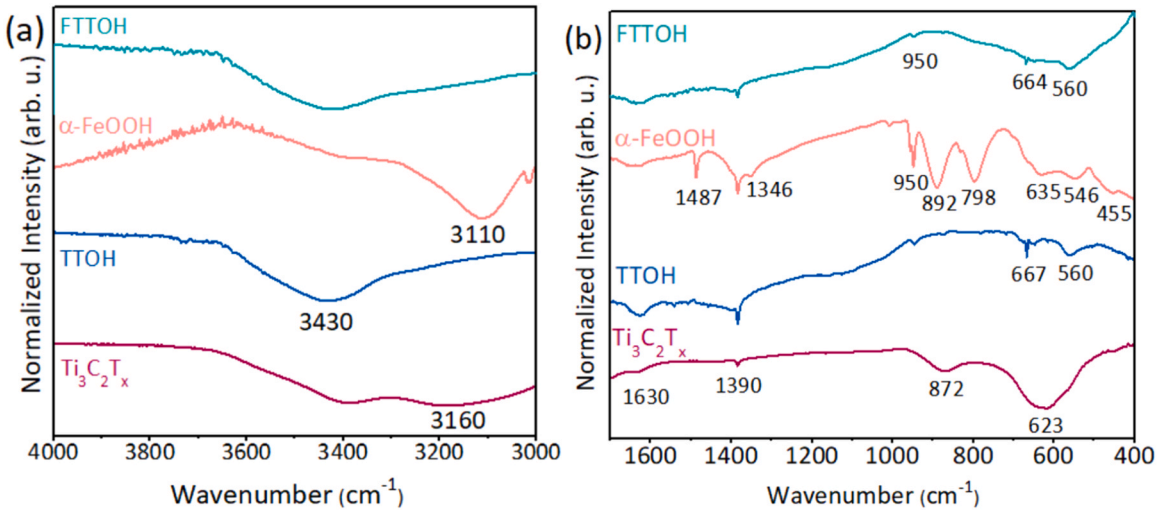

Fig. 3. FTIR spectra of $Ti_3C_2T_x$, TTOH, α-FeOOH and FTTOH samples.

896 cm^{-1} and 798 cm^{-1} can be assigned to Fe-O-OH bending vibration in α-FeOOH (Fig. 3b) [27]. In addition, compared to TTOH, FTTOH exhibits a significantly more intense and broader absorption band in the 400–700 cm^{-1} region, reflecting modified local vibrational modes due to α-FeOOH intercalation. This enhanced adsorption is attributed to additional metal-oxygen-fluoride interactions and Fe-O stretching modes α-FeOOH [29]. While both TTOH and FTTOH samples retain core MXene surface features, α-FeOOH intercalation enriches the chemical environment, particularly impacting lattice vibrations linked to transition metal and halide bonding. Based on FTIR studies combined with XRD analysis, the results confirm that α-FeOOH intercalation modifies the surface chemistry and metal coordination of $Ti_3C_2T_x$ MXene, which can significantly enhance its catalytic performance by tuning the active sites and improving interactions with reagents.

The SEM images of $Ti_3C_2T_x$ reveals the multilayered structure characteristic of the MXene, while α-FeOOH exhibits homogeneous granular morphology (Figure S2a and S2b) [32]. The SEM micrographs of TTOH and FTTOH show that both samples retain the characteristic layered MXene morphology[32]; however, α-FeOOH intercalation induces notable morphological changes (Figure S2). The TTOH sample displays well-defined, stacked, and relatively smooth sheets, indicative of effective exfoliation and interlayer expansion (Figure S2c and S2d) [26]. In contrast, the FTTOH sample exhibits increased fragmentation, and granular features, suggesting partial disruption of the layered structure and incorporation of α-FeOOH species (Figure S2c and S2d). These morphological modifications are expected to increase the surface area and active site density, potentially benefiting catalytic performance.

TEM images of FTTOH show $Ti_3C_2T_x$ MXene nanosheets covered with α-FeOOH particles (Fig. 4a and b). The MXene particles, which crystallize in a hexagonal symmetry with space group *$P6_3/mmc$* (Fig. 4c), exhibit a size ranging from hundreds of nanometers to micrometers, while the α-FeOOH nanoparticles have diameters between 2.5 and 30 nm and tend to agglomerate on the MXene surface. Energy-dispersive X-ray spectroscopy (EDS) confirmed the presence of $Ti_3C_2T_x$ with Fe content, which is close to the nominal value of 2.93 wt% (Figure S3). The high C content indicates an intact MXene backbone, while the presence of O reflects surface terminations or minor oxidation (Figure S3). Selected area electron diffraction (SAED) pattern confirms the hexagonal symmetry of the MXene, with interplanar distances of 2.66 Å and 1.53 Å for the (*100*) and (*110*) planes, respectively (Fig. 4c) [33]. Additional peaks at distances of 3.52 Å and 1.89 Å corresponds to the (*011*) and (*020*) planes of anatase TiO_2, likely due to surface oxidation (Fig. 4c) [34]. HRTEM image of α-FeOOH particles in FTTOH (Fig. 4d) reveals a region with relatively low particle density. The corresponding FFT pattern confirms peaks with hexagonal symmetry of $Ti_3C_2T_x$, corresponding to the (*100*) and (*110*) planes (Fig. 4e). In addition to these MXene-related reflections, prominent peaks are observed at distances of 3.37 Å and 1.69 Å, aligned along a common direction in the FFT. These peaks can be indexed to the (*120*) and (*240*) planes of α-FeOOH [35]. An HRTEM image acquired from a region containing agglomerated α-FeOOH particles (Figure S4a) confirmed the identification of goethite phase (Figure S4b). The radial profile of the corresponding FFT shows good agreement with the calculated powder diffraction pattern, thus supporting this assignment (Figure S4b and S4c).

The porous properties of the TTOH and FTTOH samples were characterized by N_2 adsorption-desorption measurements at 77 K. The corresponding isotherms, pore size distribution (PSD) curves, BET areas,

Table 1
Porous properties of the TTOH and FTTOH samples derived from nitrogen physisorption at 77 K.

Sample	BET area ($m2\ g^{-1}$)	Micropore volume ($cm^3\ g^{-1}$)	Mesopore volume ($cm^3\ g^{-1}$)	Porosity
TTOH	21.3	0.003	0.047	Mesoporous
FTTOH	71.2	0.009	0.131	Mesoporous

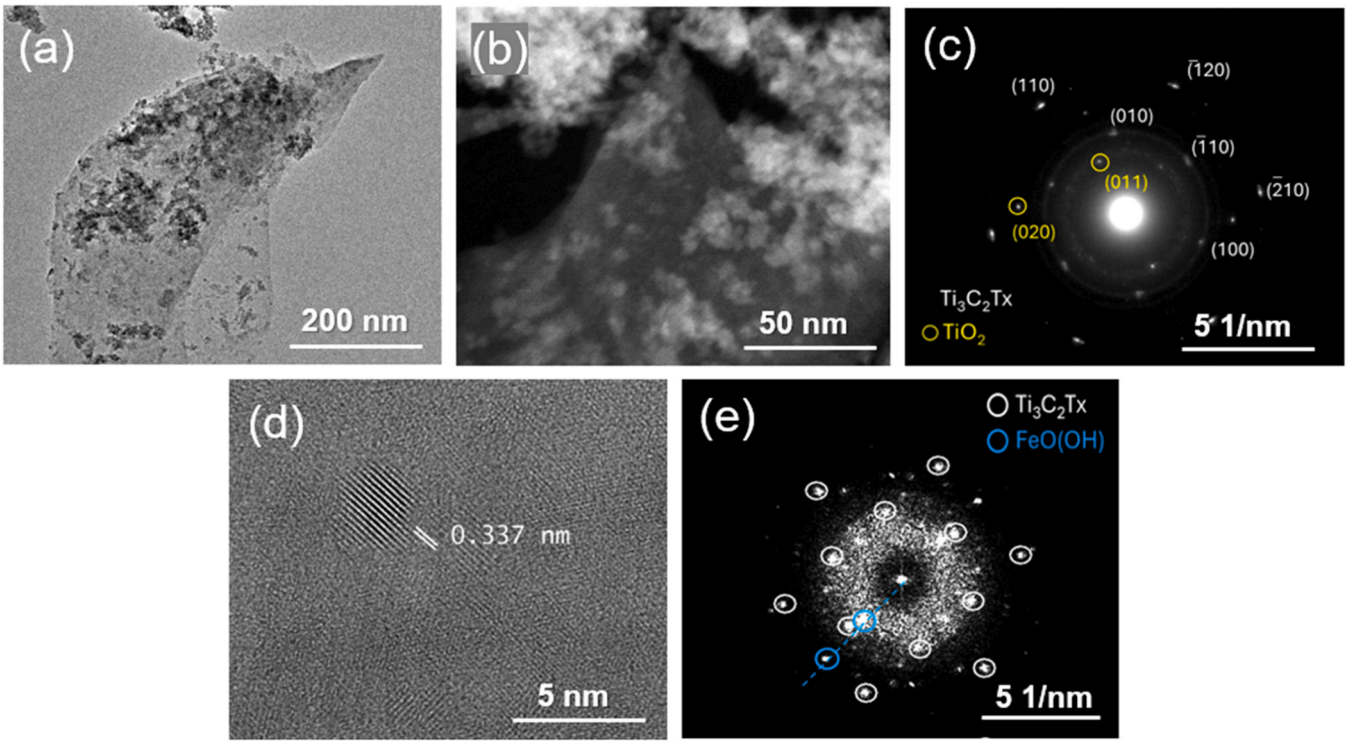

Fig. 4. (a) TEM and (b) STEM images of FTTOH with $Ti_3C_2T_x$ MXene and iron oxide particles distributed across its surface. (c) Measured SAED pattern: the indexed spots of the MXene have hexagonal symmetry and are oriented along the [001] zone axis. TiO_2 peaks are present due to surface oxidation. (d) HRTEM image of the MXene covered with iron oxide particles, along with (e) FFT pattern. The hexagonal symmetry spots in the white circles belong to the MXene ($Ti_3C_2T_x$), the spots in the blue circles corresponds to α-FeOOH, with a measured interlayer distances of 0.337 nm and 0.169 nm.

and micro- and mesopore volumes are presented in Figure S5 and Table 1. Compared with pristine multilayer MXene (8.2 m^2 g^{-1}) [36], the TTOH sample exhibited a markedly higher BET surface area of 21.3 m^2 g^{-1} (Table 1). This enhancement can be attributed to the TMAOH-assisted exfoliation and surface functionalization of MXene layers, which increases interlayer spacing and exposes more surface. The interlayer spacing is predominantly mesoporous in nature, as indicated by a mesopore volume of 0.047 cm^3 g^{-1} and a broad PSD within the mesopore range, while microporosity is negligible. Upon α-FeOOH intercalation (FTTOH sample), the porous characteristics further improved approximately threefold, with the BET area increasing to 71.2 m^2 g^{-1} and mesopore volume to 0.131 cm^3 g^{-1}, while maintaining a broad PSD [37]. This substantial increase in the porous properties is ascribed to insertion of α-FeOOH nanostructures between $Ti_3C_2T_x$ layers, which effectively prevents layer restacking and promotes the formation of additional mesopores. These results confirm that both TMAOH exfoliation and α-FeOOH intercalation significantly enhance the surface area compared to pristine MXene and α-FeOOH.

The insights into surface chemistry of FTTOH material is provided by XPS analysis which detects signals from the depth of approximately 8 nm below the material interface. To compare the evolution of surface chemistry after preparation of FTTOH material, the comparison with core-level spectra of pristine TTOH and α-FeOOH materials are presented in Fig. 5. Wide spectra (Figure S6) of all materials represent the elemental composition on the surface with the atomic concentration (at %) of each element presented in Table S4. The C 1 s spectrum (Fig. 5a) confirmed the presence of C−Ti backbone forming the $Ti_3C_2T_x$ MXene with the signal located at 282.0 eV. The C 1 s signals at ≈ 285.1 eV, ≈ 286.5 eV, ≈ 287.7 eV, and ≈ 289.0 eV are ascribed to C−C/C−H, C−O, C═O, and O−C═O bonds forming adventitious carbon or hydrocarbon contaminants [38]. Signal from C−C/C−H species can be overlapped with the signal from graphitic carbon which can exists in MXene materials [39]. C 1 s signal at ≈ 292.3 eV is ascribed to surface CF_3 contaminant consistent with the F 1 s signal (Fig. 5c) detected at ≈ 689.5 eV [40]. The fundamental atomic environment of Ti atoms in FTTOH was similar to TTOH with additional surface species as apparent

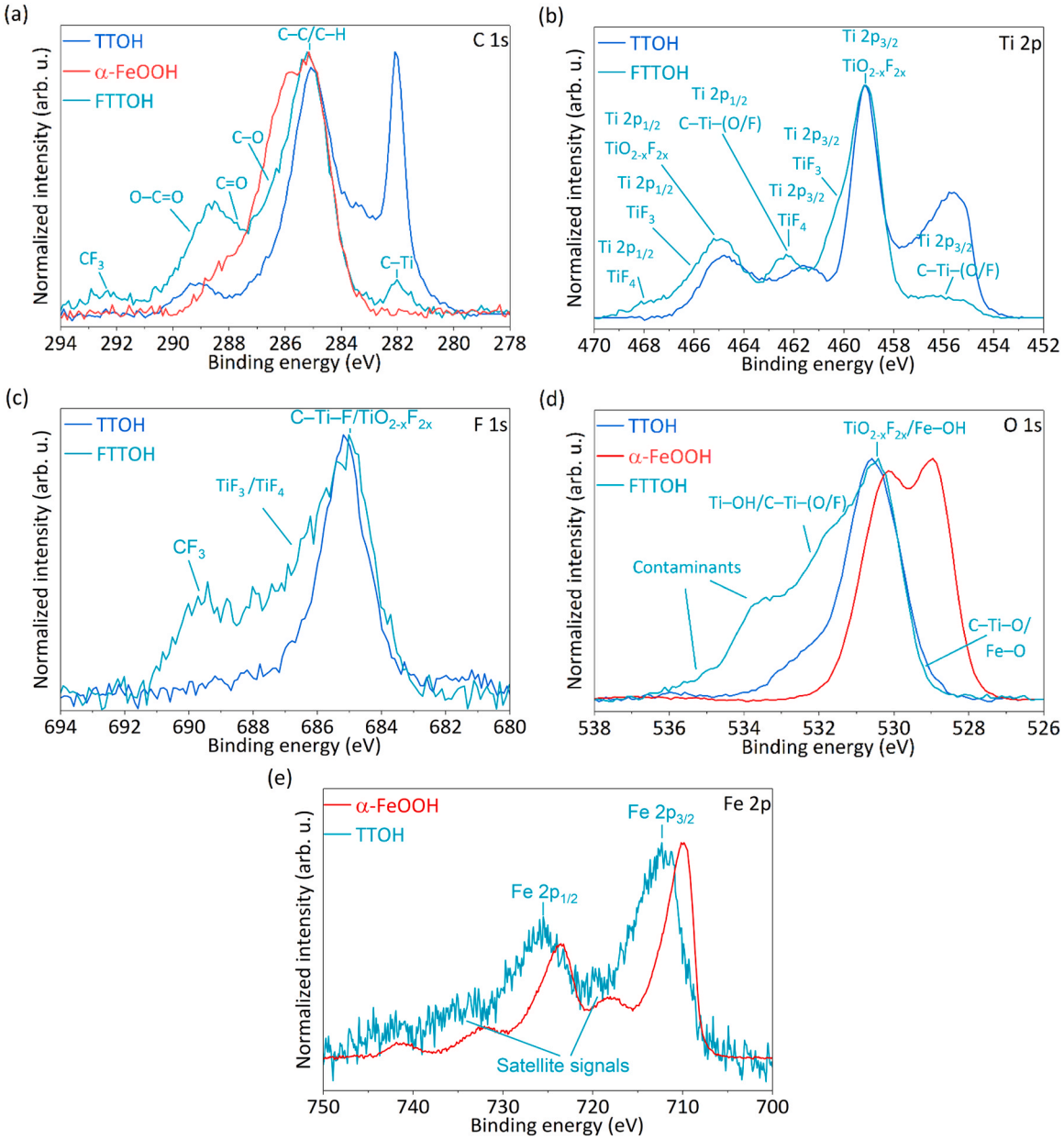

Fig. 5. XPS core-level spectra of TTOH, α-FeOOH and FTTOH: (a) C 1 s, (b) Ti 2p, (c) F 1 s, (d) O 1 s, and (e) Fe 2p.

from the Ti 2p spectra in Fig. 5b. Broad Ti $2p_{3/2}$ signal at ≈ 456.0 eV (and $2p_{1/2}$ signal at ≈461.8 eV) with low intensity corresponds to minor concentration of surface terminations bonded on surface as C−Ti−(O/F), where O/F denotes mixed contribution from oxygen and/or fluorine elements as discussed in work by Natu et al [19]. Contribution of surface oxide in the form of TiO_2 most likely dopped with fluorine forming the compound with general formula $TiO_{2-x}F_{2x}$ implies from the Ti $2p_{3/2}$ signal detected at ≈ 459.2 eV (and Ti $2p_{1/2}$ at ≈465.0 eV) [19]. The presence of C−Ti−F terminations and $TiO_{2-x}F_{2x}$ oxide on the surface is consistent with the F 1 s signal at ≈ 685.0 eV (overlapping signals denoted in F 1 s spectrum as C–Ti–F/$TiO_{2-x}F_{2x}$). Other signals contributing to the Ti 2p spectra are resolved at ≈ 460.2 eV (Ti $2p_{3/2}$ signal, and corresponding ≈466.0 eV position of Ti $2p_{1/2}$ signal) and ≈ 462.2 eV (Ti $2p_{3/2}$ signal, and corresponding ≈468.0 eV position of Ti $2p_{1/2}$ signal) which are most likely ascribed to TiF_3 and TiF_4 materials [41-43]. The overlapped signal from TiF_4 and TiF_3 (TiF_4/TiF_3) is detected in F 1 s spectrum (Fig. 5c) at position ≈ 686.6 eV [41]. With respect to the detected concentration of Fe and Ti elements of ≈ 5.5 at% and ≈ 16.0 at %, respectively (Table S4), and pattern of detected Ti 2p and Fe 2p spectra (Fig. 5b and e), it is apparent that the $Ti_3C_2T_x$ MXene and mostly $TiO_{2-x}F_{2x}$ oxide are the predominant phases on the FTTOH surface. Therefore, these materials are expected to significantly contribute to the signal of O 1 s spectrum (Fig. 5d). The O 1 s spectra measured for pristine α-FeOOH (Fig. 5a) are consistent with the previously published

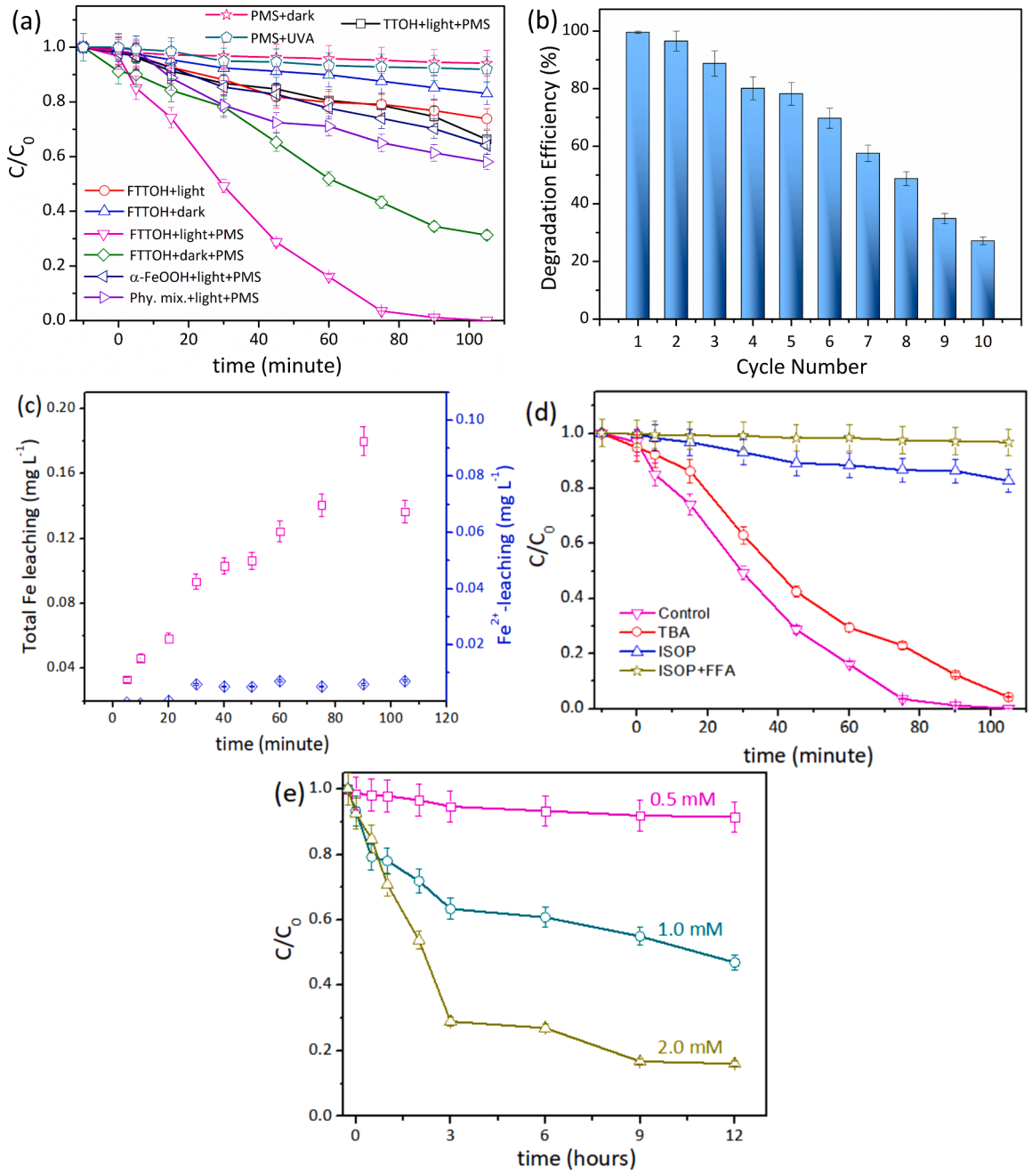

Fig. 6. Fig. 6. (a) CAF degradation profiles using Ti3C2Tx (MXene), TTOH, α-FeOOH, FTTOH and their physical mixture under varying light and PMS conditions. (b) Reusability of FTTOH/Light/PMS over ten cycles, (c) Total Fe (Fe(II)+Fe(III)) leaching and Fe(II) leaching from FTTOH under UVA/PMS. (d) Effect of radical scavengers (TBA, IPA, IPA+FFA) on CAF degradation, confirming active species involvement. Initial conditions: [CAF] = 50 μM; [Catalyst] = 0.2 g L-1; [PMS] = 0.5 mM. (e) Degradation extent of CAF in real wastewater (WW) using FTTOH under UVA with varying PMS concentrations after 12 h. Initial conditions: [FTTOH] = 0.2 g L-1, [CAF] = 50 μM.

results and the signals at ≈ 528.9 eV and ≈ 530.2 eV are assigned to Fe in lattice of material (Fe–O), and lattice OH- group (Fe–OH) [44]. These O 1 s signals overlap the position originating from species in MXene: the surface terminations bonded as C–Ti–O at position ≈ 529.1 eV [19], resulting overlapped signals denoted as C–Ti–(O)/Fe–O; and lattice oxygen in $TiO_{2-x}F_{2x}$ at ≈ 530.5 eV [19], resulting signal denoted as $TiO_{2-x}F_{2x}$/Fe–OH. The asymmetric signal detected in TTOH positioned around ≈ 532.1 eV contribute to the spectra of FTTOH due to the surface species bonded as C–Ti–(O/F) [19] and is overlapped with the signal which is detected in $TiO_{2-x}F_{2x}$ materials [45,46]. Unfortunately, the O 1 s signal is overlapped with the signals originating from C–O, C═O, and O–C═O species forming adventitious carbon or hydrocarbon contaminants (or other contaminants) and this contribution is herein not negligible as apparent from significant share of these signals in C 1 s spectra, making resolving of shares the signals from TTOH and α-FeOOH challenging. Among the other contaminants, which contributed to the O 1 s signal of FTTOH, are adsorbed water (signal at ≈533.5 eV) and other organic impurities (signal at ≈535.2 eV) signals denoted as contaminants [19]. The Fe 2p signal detected for pristine α-FeOOH (Fig. 5e) with the binding energy positions of main Fe $2p_{3/2}$ and Fe $2p_{1/2}$ signals at ≈ 709.9 eV and 723.5 eV [47], respectively, was significantly shifted towards higher binding energy by ≈ 2.2 eV ascribed to changes in the close proximity of Fe atoms after incorporation the α-FeOOH to the FTTOH surface [48].

3.2. Catalytic performance

The catalytic performance of the FTTOH catalyst toward CAF degradation *via* PMS activation was assessed under optimized conditions. CAF degradation was compared between the different systems including $Ti_3C_2T_x$, TTOH, α-FeOOH and FTTOH, with particular emphasis on the role of UVA light and PMS (Fig. 6a). Control experiments with FTTOH under light without PMS (0.0032 min^{-1}) and in dark with PMS (0.0018 min^{-1}), showed only minor activity (Fig. 6a). Among all tested systems, FTTOH/Light/PMS exhibited the highest degradation efficiency, achieving a rate constant of 0.0442 min^{-1}, which was significantly higher than FTTOH/Dark/PMS (0.0111 min^{-1}), thus highlighting the crucial role of the UVA light. Compared to $Ti_3C_2T_x$/Light/PMS (0.0007 min^{-1}), α-FeOOH/Light/PMS (0.0041 min^{-1}), TTOH/Light/PMS (0.0036 min^{-1}) and a physical mixture of the TTOH with α-FeOOH under Light/PMS (0.0056 min^{-1}), the FTTOH/Light/PMS system exhibited significantly higher performance, suggesting the importance of the increased surface area brought by expansion of the MXene interlayer spacing and confirming a synergy between FTTOH and α-FeOOH (Figure S7). This synergy can be ascribed to dispersion of Fe sites in α-FeOOH on $Ti_3C_2T_x$ MXene, which facilitate PMS activation through Fe^{3+}/Fe^{2+} cycling, where UVA light promotes the photoreduction of Fe^{3+} to Fe^{2+} along with electron transfer between MXene and iron sites, improving charge carriers' lifetime. Therefore, it accelerates the generation of ROS responsible for CAF degradation. The synergistic effect (SE) can be calculated by using Equation 1 (where k' is apparent rate constant), yielding a value of 10.8, which represents a remarkable enhancement compared with similar Fe-containing systems reported in the literature.

$$SE\ (light) = \frac{k'_{UVA+PMS+FFTOH}}{k'_{UVA} + k'_{PMS} + k'_{FFTOH}} \quad (1)$$

For instance, Golshan et al. reported SE values of 1.5 for $CuFe_2O_4$ in the UV/PMS systems [49]. Similarly, Tian et al. observed SE values as high as 2.1 for ZnO@spinel cobalt ferrite@carbon nanotube under UVC/PMS conditions [50]. This comparison clearly shows that the current system confirms MXene has a crucial role in the enhanced synergy by combining its conductive properties to the Fenton properties of α-FeOOH, thus promoting the generation of ROS.

3.3. FTTOH as potential stable Fenton catalyst

The reusability of the FTTOH catalyst was evaluated over ten consecutive cycles to assess its operational stability (Fig. 6b). CAF degradation efficiency remained high at approximately **80%** during the first five cycles and gradually decreased to about **30%** after ten cycles. This decline can be ascribed to partial deactivation of catalytic surface by fouling or partial oxidation as demonstrated in XPS (Fig. 5) [51]. However, this decrease is not due to iron leaching since a minimal release of Fe was observed (0.18 mg L^{-1} while employing 0.2 L^{-1} of FTTOH). This amount of leached iron corresponds to only **3.07%** of the total nominal iron content (0.293 mg Fe in 10 mg FTTOH) intercalated in the MXene, indicating a low degree of leaching and high structural stability of the FTTOH catalyst (Table S3). To check this point, the XRD, FTIR and TEM characterization of the FTTOH catalyst before and after CAF degradation experiments was compared. The post-degradation XRD pattern shows diminished intensity of the (*002*) reflection and higher-angle peaks, indicating loss of long-range order and decreased crystallinity (Figure S8) [52]. This arises from partial oxidation and structural disorder, which disrupt the interlayer spacing and Fe-O-Ti coordination. New peaks attributed to anatase TiO_2 also appear, including the (*101*) reflection at 25.28 ° and a weaker feature near 48.37 ° (likely the (*200*) peak), consistent with XPS analysis (Figure S8) [53]. In the FTIR spectra after CAF degradation, the intensity of the -OH stretching and H-O-H bending modes decreases significantly (Figure S9). This observation suggests that surface hydroxyl groups (-OH) play an important role in PMS activation, accompanied by changes in the catalysts's surface properties [54]. The band around 1068 cm^{-1}, attributed to C-O stretching vibrations, becomes sharper, indicating an increased amount of residual oxygen-containing species, possibly from adsorbed CAF degradation products [55]. The Ti-F vibrational band shifts noticeably from 950 to 750–700 cm^{-1} region, consistent with coexistence of Ti, -O, and -F species in the MXene interlayer galleries [29]. Additionally, broadening of the FTIR features in the 400–700 cm^{-1} region after CAF degradation is likely caused by several factors including enhanced surface oxidation, formation of mixed Ti/Fe oxides/hydroxides, and increased structural disorder, thus contributing to overlapped and broadened metal-oxygen vibrational bands [56]. The TEM performed after 10 cycles of CAF degradation revealed higher particle contamination, primarily in particle centers with cleaner edges (Figure S10a), while the overall morphology of the FTTOH particles remained unchanged (Figure S10b), with MXene $Ti_3C_2T_x$ sheets covered by α-FeOOH nanoparticles. No significant changes in the nanoparticle crystallinity were observed post-degradation. $Ti_3C_2T_x$ crystals oriented along the [001] zone axis, with *d*-spacings of 2.66 Å and 1.53 Å measured for the (*100*) and (*110*) planes, respectively. For the agglomerated particles (Figure S10c), interplanar spacings of 3.37 Å, 2.45 Å, and 1.69 Å, corresponding to the (*120*), (*111*), and (*240*) planes of the goethite, were measured from the FFT. These values are consistent with those of the fresh catalyst, indicating no significant structural degradation during the TEM investigation.

Therefore, FTTOH cannot be considered as reusable catalyst due to these changes at its surface, especially the partial oxidation of MXene. On the other hand, the iron leaching is remarkably low, suggesting FTTOH is promising for further development as stable Fenton catalyst which is one of the key discoveries of the present work. Indeed, Fenton-based processes (either homogeneous or heterogeneous) usually suffer of long-term stability and efficiency in waters treatment. To confirm the robustness of heterogeneous Fenton reactions triggered by FTTOH, the potential contribution of homogeneous reactions from the leached iron was assessed. To this end, a system containing 1.14 mg L^{-1} of Fe $(ClO_4)_3{\cdot}xH_2O$ (corresponding to 0.18 mg L^{-1} Fe, equivalent to amount of iron leached from FTTOH) in 50 mL of CAF solutions was prepared. Under UVA/PMS conditions, this system led to approximately **10%** degradation within 120 min (Figure S11), demonstrating that heterogeneous Fenton process is predominant in the FTTOH/Light/PMS

system. In addition, the CAF degradation performance, catalysts reusability, and iron leaching of FTTOH were compared with those of conventional Fe_2O_3 and Fe_3O_4 prepared under our laboratory conditions via a solvothermal method (Figure S12a) [57,58]. The degradation efficiency of Fe_2O_3 decreased from **34%** to **27%**, while that of Fe_3O_4 declined from **67%** to **42%** after just two consecutive cycles (Figure S12b), suggesting significant Fe leaching. These results further confirm the superior degradation performance, good reusability, and high structural stability of FTTOH. Therefore, MXene has been proven here to stabilize the iron species *via* intercalation, thus providing stable and efficient active sites to trigger Fenton-based processes and degrade organic pollutants. However, the surface oxidation of MXene upon reuse should be addressed to make it more robust before considering such hybrid MXene-Fenton catalysts as potential sustainable materials for wastewaters treatment.

3.4. Mechanistic insights into PMS activation

To elucidate the activation of PMS using FTTOH catalyst, the ROS responsible for CAF degradation have been identified using scavenging studies in the presence of TBA, ISOP, and a mixture of FFA+ISOP (Fig. 6d). The degradation rate constants significantly decreased from 0.0442 min^{-1} to 0.0252 min^{-1}, 0.0017 min^{-1}, and 0.0003 min^{-1}, respectively, indicating that both $^{\bullet}OH$ and $SO_4^{\bullet-}$ radicals are the predominant ROS. The quantitative contribution of the identified ROS using Eqs. S1-S3 (Text S3) were **42.98%** for $^{\bullet}OH$, **53.16%** for $SO_4^{\bullet-}$ and **2.9%** for $^1O_2$. Therefore, the PMS activation leads to a radical-mediated CAF degradation. Furthermore, the complete consumption of PMS during CAF degradation (Figure S13) confirms the ROS generation is from the PMS activation, suggesting a high density of Fenton active sites on the surface of FTTOH [59].

Indirect EPR techniques, including spin trapping and oxidation of sterically hindered amines, were employed to detect and identify transient radical species in an aerated aqueous dispersion of the FTTOH catalyst. Fig. 7 shows EPR spectra recorded before and during continuous 365 nm LED irradiation of the aerated FTTOH suspension in the presence of PMS with 5,5-dimethyl-1-pyrolline N-oxide (DMPO, Fig. 7a) and 5-tert-butoxycarbonyl-5-methyl-1-pyrroline N-oxide (BMPO, Fig. 7b). In both systems, EPR signals were observed prior to irradiation, and their intensities increased markedly upon 365 nm illumination under the given experimental conditions.

The simulation analysis in the reaction system after LED@365 nm exposure with DMPO (Figure S14a) showed the formation of followed spin-adducts, $^{\bullet}$DMPO-OH ($a_N = 1.505$ mT, $a_H^{\beta} = 1.470$ mT, $g = 2.0057$; c_{rel} = **57%**) and $^{\bullet}$DMPO-SO_4^- ($a_N = 1.377$ mT, $a_H^{\beta} = 1.005$ mT, $a_H^{\gamma 1} = 0.141$ mT, $a_H^{\gamma 2} = 0.073$ mT, $g = 2.0056$; c_{rel} = **43%**). The same species were detected in the reaction system with BMPO (Figure S14b), $^{\bullet}$BMPO-OH(I) ($a_N = 1.444$ mT, $a_H^{\beta} = 1.590$ mT, $a_H^{\gamma} = 0.070$ mT, $g = 2.0057$; c_{rel} = **13%**), $^{\bullet}$BMPO-OH(II) ($a_N = 1.419$ mT, $a_H^{\beta} = 1.271$ mT, $a_H^{\gamma} = 0.065$ mT, $g = 2.0057$; c_{rel} = **47%**) and $^{\bullet}$BMPO-SO_4^- ($a_N = 1.301$ mT, $a_H^{\beta} = 0.915$ mT, $a_H^{\gamma 1} = 0.140$ mT, $a_H^{\gamma 2} = 0.079$ mT, $g = 2.0056$; c_{rel} = **40%**), and the different substituents in position 5 on BMPO moiety resulted in the formation of two diastereoisomers of $^{\bullet}$BMPO-OH spin-adduct [60,61]. Generation of such spin-adducts were expected with the major pathway of spin-adducts $^{\bullet}$DMPO-OH and $^{\bullet}$DMPO-SO_4^- generation *via* genuine spin trapping – reaction of $^{\bullet}OH$ or $SO_4^{\bullet-}$ with spin trap moiety. This also correlates with the proposed mechanism (Eq. 1-3), where the Fe^{3+} ions react with PMS resulting in $SO_4^{\bullet-}$ and subsequent $^{\bullet}OH$ formation in dark. Upon LED@365 nm exposure the homolytic cleavage of -O-O- in PMS served as an additional source of these radical species. These observations were further confirmed using the BMPO spin trap, where the same radical species were detected with a similar relative ratio of oxygen-centered to sulfur-centered spin adducts as in the DMPO system. Control experiments without PMS showed only negligible spin-adduct formation in the aerated FTTOH/DMPO system (data not shown), consistent with the Fig. 6a.

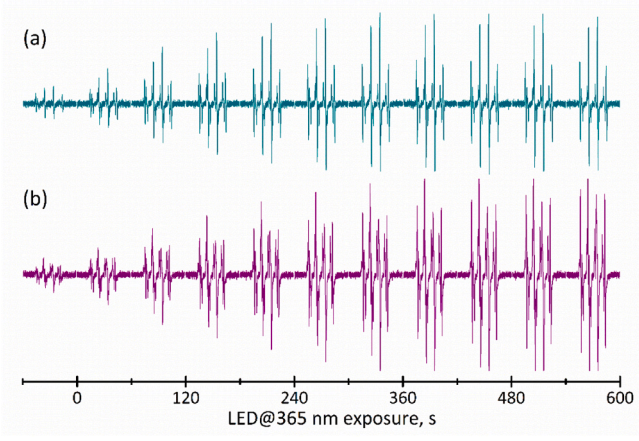

Fig. 7. The sets of individual EPR spectra (magnetic field sweep width, SW = 9 mT) monitored upon continuous LED@365 nm exposure (irradiance 15 cm^{-2}) of aerated aqueous suspension of FTTOH in the presence in the presence of PMS and (a) DMPO or (b) BMPO spin trapping agent. Initial concentrations: c (TFFOH) = 0.4 mg mL^{-1}, c_0(PMS) = 0.5 mM, c_0(DMPO) = 42 mM, c_0(BMPO) = 10 mM.

The oxidation of sterically hindered amine 4-oxo-2,2,6,6-tetramethylpiperidine (Temp) in FTTOH/PMS system was also realized using EPR spectroscopy. Fig. 8 shows EPR spectra recorded before and during continuous 365 nm LED irradiation of aerated aqueous PMS/Temp (Fig. 8a) and FTTOH/PMS/Temp (Fig. 8b) systems. In both cases, the characteristic three-line EPR signal of the stable nitroxide radical 4-oxo-2,2,6,6-tetramethylpiperidin-1-oxyl (Tempone) was observed, with hfcc parameters $a_N = 1.613$ mT, $a_{13\,C}$ ($6x^{13}C$) = 0.583 mT and $g = 2.0057$. Upon LED@365 nm irradiation, Tempone EPR intensity increased in both systems, confirming efficient oxidation of Temp, confirming the efficient generation of reactive species ($^{\bullet}OH$, $SO_4^{\bullet-}$, and $^1O_2$) in the FTTOH/PMS system [60]. Comparison of systems with and without FTTOH revealed a significant decrease in EPR intensity in the presence of the catalyst, attributed to the role of Fe^{3+} ions, which also oxidize Temp to Tempone, supporting the Fenton-like catalytic behaviour of FTTOH.

Based on the above-mentioned data, a plausible mechanism for PMS activation over the FTTOH catalyst under UVA irradiation is proposed (Fig. 9). In this system, UVA light plays a significant role in promoting PMS activation through the photolysis of surface Fe species, regenerating Fe^{2+} from Fe^{3+}. The FTTOH catalyst exhibiting higher surface area is triggering Fenton-based reactions by the activation of PMS reactions (Eqs. 2-4) [62,63]. The surface complexation between PMS on FTTOH can be considered (Eq. 2), thus leading to a change in the surface oxidation state and reduction of Fe^{3+} to Fe^{2+} [64-67]. This step aligns with pre-reaction XPS confirming active Fe sites and post-reaction FTIR showing decreased -OH groups.

The generated Fe^{2+} also activates PMS into $SO_4^{\bullet-}$ (Eq. 3), while $SO_4^{\bullet-}$ can be converted into $^{\bullet}OH$ by reaction with water (Eq. (4)) [64-67]. These radicals has been identified as the predominant ROS. In parallel, PMS can undergo self-decomposition to produce $^1O_2$, which further contributes to pollutant degradation [64,65]. The generation of ROS and the participation of Fe-centred redox cycles are confirmed by EPR spin-trapping and Temp oxidation experiments. Moreover, the intrinsically high electrical conductivity and tunable surface chemistry of $Ti_3C_2T_x$ MXene facilitate efficient charge carrier separation and transfer, thereby enhancing ROS generation [68].

$$+ HSO_5^- + \quad Fe^{3+} + HSO_5^- \rightarrow Fe^{2+} + SO_5^{\bullet-} + H^+ \qquad (3)$$

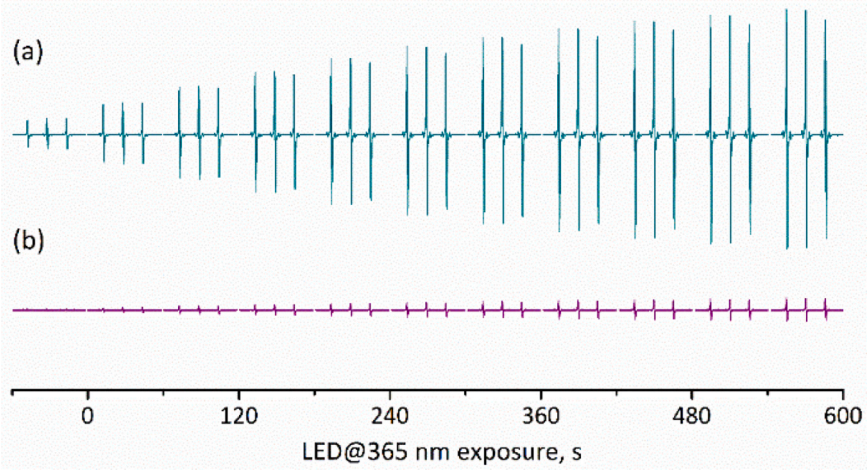

Fig. 8. The sets of individual EPR spectra (magnetic field sweep width, SW = 6 mT) monitored upon continuous LED@365 nm exposure (irradiance 15 cm^{-2}) of aerated aqueous system containing Temp and PMS (a) without catalyst and (b) with TFFOH catalyst. Initial concentrations: c(TFFOH) = 0.4 mg mL^{-1}, c_0(PMS) = 0.5 mM, c_0(Temp) = 0.5 mM.

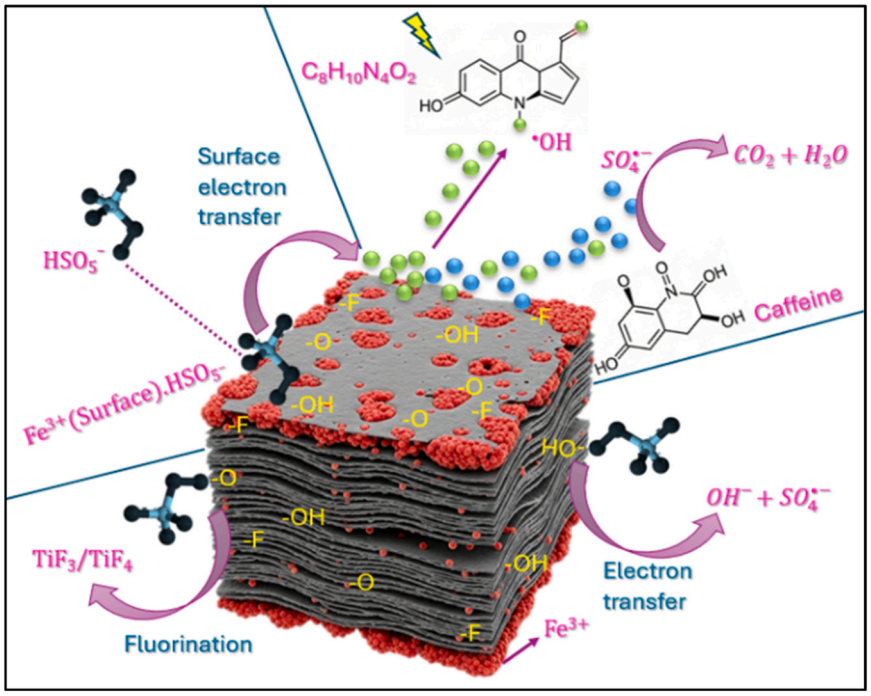

Fig. 9. Proposed mechanism of CAF degradation via PMS activation using FTTOH catalysts.

$$Fe^{2+} + HSO_5^- \rightarrow Fe^{3+} + SO_4^{\bullet-} + OH^- \quad (4)$$

$$SO_4^{\bullet-} + H_2O \rightarrow SO_4^{2-} + {}^{\bullet}OH \quad (5)$$

This proposed mechanism aligns with the structural and vibrational changes observed in the XRD and FTIR analyses before and after CAF degradation (Figure S8 and S9), supporting the occurrence of surface modifications during the reaction. Overall, the proposed PMS activation mechanism highlights the critical role of surface chemistry modulation and the stabilizing effect of MXene on Fenton active sites. The synergistic interplay between Fenton active sites and the surface chemistry of $Ti_3C_2T_x$ MXene results in a stable and efficient catalyst capable of efficent PMS activation and CAF degradation under UVA irradiation.

3.5. Evaluation of FTTOH/PMS system in real wastewaters

To assess the practical applicability of FTTOH/PMS system, CAF degradation was conducted in tertiary effluent collected from a municipal WWTP in Bratislava (Table S5). Under optimized conditions, only ~ **10%** CAF removal was achieved in wastewater after 12h(Fig. 6e). The reduced catalytic performance (compared to deionized water) can be attributed to light attenuation by suspended matter and competitive between PMS and generated ROS with coexisting organic and inorganic constituents [69,70]. Additional experiments were performed by increasing the PMS dosages, that markedly enhanced CAF removal, reaching up to **84%** degradation with 2 mM PMS (Fig. 6e). These results demonstrate that FTTOH remains catalytically active in real water matrices, supporting its potential applicability for PMS activation and warranting further investigations of such hybrid MXene/Fenton

catalysts toward scale-up implementation.

As environmental safety considerations are also important to consider, we have been recently evaluated the ecotoxicity of $Ti_3C_2T_x$ MXene material in aquatic systems using the freshwater alga *S. quadricauda* as a bioindicator [71]. While a detailed ecotoxicological assessment is beyond the scope of this study, which focuses on stabilizing Fenton-like catalytic sites, these efforts aim to support the safe deployment of hybdrid MXene/Fenton-assisted AOPs.

4. Conclusions

This work demonstrates that α-FeOOH intercalation into $Ti_3C_2T_x$ MXene (FTTOH) produces an efficient heterogeneous Fenton-like catalyst for PMS activation under UVA irradiation. The intercalation-driven expansion of the MXene interlayers and the resulting increase in surface area (from 21.3 m^2 g^{-1} to 71.2 m^2 g^{-1} after α-FeOOH intercalation), significantly enhance the accessibility and utilization of Fenton-active sites, enabling complete CAF degradation within 90 min at low iron-loading with minimal metal leaching of 3.07 wt%. These characteristics directly address the major limitations of conventional Fenton processes, including secondary pollution (iron sludge), catalyst stability and operational costs, thereby underscoring the potential of hybrid MXene/Fenton catalysts.

Beyond this specific system, the findings establish that MXenes as a versatile platform for heterogeneous Fenton catalysis. However, the surface oxidation of the MXene matrix should be addressed in future studies where exploration of alternative MXene compositions and other Fenton-active metals can be considered. Finally, the present study suggests hybrid MXene/Fenton heterogenous catalysts are encouraging for potential application in wastewaters treatment.

CRediT authorship contribution statement

Shalu Atri: Conceptualization – Investigation – Methodology – Writing: original draft – Writing: review & editing – Funding acquisition; **Hamidreza Behtooei**: Writing: original draft – Writing: review & editing; **Mario Kotlar:** Investigation – Methodology; **Frantisek Zazimal:** Investigation – Methodology – Writing: review & editing – Funding acquisition; **Dana Dvoranova:** Investigation – Methodology – Writing: review & editing; **Tomas Roch:** Investigation – Methodology; **Leonid Satrapinskyy:** Investigation – Methodology; **Tomas Zelenka:** Investigation – Methodology; **Tomas Homola:** Writing: review & editing; **Olivier Monfort:** Conceptualization – Methodology – Supervision – Writing: original draft – Writing: review & editing – Funding acquisition.

Declaration of Competing Interest

The authors declare that they have no known competing financial interests or personal relationships that could have appeared to influence the work reported in this paper.

Acknowledgements

This work has been carried out in the frame of the PhotoMXene project no. 3305/03/02, co-funded by the EU Horizon 2020 Research and Innovation Program under the SASPRO2 COFUND Marie Sklodowska-Curie Action grant agreement no. 945478. This work was also partially financed by the Slovak Research and Development Agency under contracts Nos. APVV-21–0039 and APVV-21–0053. The research infrastructure was also partially supported by projects LM2023039 and LM2023051 funded by the Ministry of Education, Youth and Sports of the Czech Republic.

Appendix A. Supporting information

Supplementary data associated with this article can be found in the online version at

Data availability

Data will be made available on request.

References

[1] K. Kosek, A. Luczkiewicz, S. Fudala-Ksiazek, K. Jankowska, M. Szopinska, O. Svahn, J. Tranckner, A. Kaiser, V. Langas, E. Bjorklund, Implementation of advanced micropollutants removal technologies in wastewater treatment plants (WWTPs)-Examples and challenges based on selected EU countries, Environ. Sci. Policy 112 (2020) 213–226.
[2] S. Li, B. He, J. Wang, J. Liu, X. Hu, Risks of caffeine residues in the environment: necessity for a targeted ecopharmacovigilance program, Chemosphere 243 (2020) 125343.
[3] C. Nebot, R. Falcon, K.G. Boyd, S.W. Gibb, Introduction of human pharmaceuticals from wastewater treatment plants into the aquatic environment: a rural perspective, Environ. Sci. Pollut. Res. 22 (14) (2015) 10559–10568.
[4] L.R. Frazao, S.B. Penninck, C.N. Signori, R. Mendes-Lopes, Pharmaceuticals, caffeine and cocaine on the coastal zone of Ubatuba (Brazil): a potential threat to photosynthetic carbon fixation, Sci. Total Environ. 973 (2025) 179167.
[5] C. Baracchini, L. Messager, P. Stocker, V. Leignel, The impacts of the multispecies approach to caffeine on marine invertebrates, Toxics 12 (1) (2024) 29.
[6] M.A. Oturan, J.J. Aaron, Advanced oxidation processes in water/wastewater treatment: principles and applications. A review, Crit. Rev. Environ. Sci. Technol. 44 (23) (2014), 2577-2264.
[7] S. Rodrigues, C. Gonçalves, O. Golovko, S.C. Antunes, Ecotoxicological impacts of caffeine on Daphnia magna: insights from acute to chronic exposures, Ecotoxicology (2025) 1–17.
[8] Office of the European Union L-, P., Luxembourg, L., 2024. DIRECTIVE (EU) 2024/3019 OF THE EUROPEAN PARLIAMENT AND OF THE COUNCIL of 27 November 2024 concerning urban wastewater treatment (recast) (Text with EEA relevance).
[9] D.T. Sponza, G. Guney, Photodegradation of some brominated and phenolic micropollutants in raw hospital wastewater with CeO_2 and TiO_2 nanoparticles, Water Sci. Technol. 76 (10) (2017) 2603–2622.
[10] X. Duan, X. Niu, J. Gao, S. Wacławek, L. Tang, D.D. Dionysiou, Comparison of sulfate radical with other reactive species, Curr. Opin. Chem. Eng. 38 (2022) 100867.
[11] R. Xiao, Z. Luo, Z. Wei, S. Luo, R. Spinney, W. Yang, D.D. Dionysiou, Activation of peroxymonosulfate/persulfate by nanomaterials for sulfate radical-based advanced oxidation technologies, Curr. Opin. Chem. Eng. 19 (2018) 51–58.
[12] S.J. Olusegun, T.G. Souza, G.D.O. Souza, M. Osial, N.D. Mohallem, V.S. Ciminelli, P. Krysinski, Iron-based materials for the adsorption and photocatalytic degradation of pharmaceutical drugs: a comprehensive review of the mechanism pathway, J. Water Proc. Eng. 51 (2023) 103457.
[13] A. Mirzaei, Z. Chen, F. Haghighat, L. Yerushalmi, Removal of pharmaceuticals from water by homo/heterogonous Fenton-type processes-A review, Chemosphere 174 (2017) 665–688.
[14] M. Naguib, M.W. Barsoum, Y. Gogotsi, Ten years of progress in the synthesis and development of MXenes, Adv. Mater. 33 (39) (2021) 2103393.
[15] J. Yin, B. Ge, T. Jiao, Z. Qin, M. Yu, L. Zhang, Q. Zhang, Q. Peng, Self-assembled sandwich-like MXene-derived composites as highly efficient and sustainable catalysts for wastewater treatment, Langmuir 37 (3) (2021) 1267–1278.
[16] V. Singh, V.C. Srivastava, Self-engineered iron oxide nanoparticle incorporated on mesoporous biochar derived from textile mill sludge for the removal of an emerging pharmaceutical pollutant, Environ. Pollut. 259 (2020) 113822.
[17] L. Zhang, D. Huang, P. Zhao, G. Yue, L. Yang, W. Dan, Highly efficient methylene blue removal by TMAOH delaminated $Ti_3C_2T_x$ MXene suspension and the mechanistic aspect, Sep. Purif. Technol. 288 (2022) 120718.
[18] G.B. Ortiz de la Plata, O.M. Alfano, A.E. Cassano, The heterogeneous photo-Fenton reaction using goethite as catalyst, Water Sci. Technol. 61 (12) (2010) 3109–3116.
[19] V. Natu, M. Benchakar, C. Canaff, A. Habrioux, S. Célérier, M.W. Barsoum, A critical analysis of the X-ray photoelectron spectra of $Ti_3C_2T_z$ MXenes, Matter 4 (4) (2021) 1224–1251.
[20] L. Zauška, T. Zelenka, E. Beňová, M. Želinská, M.Č. Hološová, V. Zeleňák, M. Bálintová, A. Eštoková, M. Almáši, From drug delivery to environmental impact: long-term behaviour of functionalized SBA-15 over a 20-year simulation, J. Environ. Chem. Eng. 13 (2025) 119561.
[21] M. Thommes, K. Kaneko, A.V. Neimark, J.P. Olivier, F. Rodriguez-Reinoso, J. Rouquerol, K.S.W. Sing, Physisorption of gases, with special reference to the evaluation of surface area and pore size distribution (IUPAC Technical Report), Pure Appl. Chem. 87 (9-10) (2015) 1051–1069.
[22] T. Zelenka, T. Horikawa, D.D. Do, Artifacts and misinterpretations in gas physisorption measurements and characterization of porous solids, Adv. Colloid Interface Sci. 311 (2023) 102831.
[23] D. Jia, O. Monfort, K. Hanna, G. Mailhot, M. Brigante, Caffeine degradation using peroxydisulfate and peroxymonosulfate in the presence of Mn_2O_3. Efficiency, reactive species formation and application in sewage treatment plant water, J. Clean. Prod. 328 (2021) 129652.
[24] L.L. Stookey, Ferrozine-a new spectrophotometric reagent for iron, Anal. Chem. 42 (7) (1970) 779–781.
[25] S. Waclawek, K. Grubel, M. Cernik, Simple spectrophotometric determination of monopersulfate, Spectrochim. Acta Part A 149 (2015) 928–933.

[26] M. Alhabeb, K. Maleski, B. Anasori, P. Lelyukh, L. Clark, S. Sin, Y. Gogotsi, Guidelines for synthesis and processing of two-dimensional titanium carbide ($Ti_3C_2T_x$ MXene), Chem. Mater. 29 (18) (2017) 7633–7644.

[27] A. Jaiswal, S. Banerjee, R. Mani, M.C. Chattopadhyaya, Synthesis, characterization and application of goethite mineral as an adsorbent, J. Environ. Chem. Eng. 1 (3) (2013) 281–289.

[28] L. Zhang, D. Huang, P. Zhao, G. Yue, L. Yang, W. Dan, Highly efficient methylene blue removal by TMAOH delaminated $Ti_3C_2T_x$ MXene suspension and the mechanistic aspect, Sep. Purif. Technol. 288 (2022) 120718.

[29] T. Parker, D. Zhang, D. Bugallo, K. Shevchuk, M. Downes, G. Valurouthu, A. Inman, B. Chacon, T. Zhang, C.E. Shuck, Y.J. Hu, Fourier-transform infrared spectral library of MXenes, Chem. Mater. 36 (17) (2024) 8437–8446.

[30] M. Hilal, W. Yang, Y. Hwang, W. Xie, Tailoring MXene thickness and functionalization for enhanced room-temperature trace NO_2 sensing, NanoMicro Lett. 16 (1) (2024) 84.

[31] H.F. Chen, G.D. Wei, X. Han, S. Li, P.P. Wang, M. Chubik, A. Gromov, Z.P. Wang, W. Han, Large-scale synthesis of hierarchical alpha-FeOOH flowers by ultrasonic-assisted hydrothermal route, J. Mater. Sci. Mater. Electron. 22 (3) (2011) 252–259.

[32] V.V. Kusumkar, S. Atri, S. İnan, M. Gregor, T. Roch, H. Makarov, M. Caplovicova, M. Galambos, E. Viglasova, G. Plesch, O. Monfort, Application of MXene for remediation of low-level radioactive aqueous solutions contaminated with ^{133}Ba and ^{137}Cs, Chem. Commun. 59 (80) (2023) 12007–12010.

[33] A. Pazniak, P. Bazhin, N. Shplis, E. Kolesnikov, I. Shchetinin, A. Komissarov, J. Polcak, A. Stolin, D. Kuznetsov, $Ti_3C_2T_x$ MXene characterization produced from SHS-ground Ti_3AlC_2, Mater. Des. 183 (2019) 108143.

[34] W. Li, Y. Bai, C. Liu, Z. Yang, X. Feng, X. Lu, N.K. Van Der Laak, K.Y. Chan, Highly thermal stable and highly crystalline anatase TiO_2 for photocatalysis, Environ. Sci. Technol. 43 (14) (2009) 5423–5428.

[35] A.M. Sudapalli, N.G. Shimpi, Hydrothermal synthesis of α-FeOOH (1D) nanorods and their transition to α-Fe_2O_3 (0D): an efficient photocatalyst in neutralizing hazardous organic dyes, N. J. Chem. 47 (30) (2023) 14323–14334.

[36] Y. Zhang, J. Luo, B. Feng, H. Xu, Y. Sun, X. Gu, X. Hu, M. Naushad, B. Gao, H. Ren, Delamination of multilayer $Ti_3C_2T_x$ MXene alters its adsorpiton and reduction of heavy metals in water, Environ. Pollut. 330 (2023) 121777.

[37] B. Jiang, S. Chen, H. Wang, J. Yan, X. Wang, X. Xu, J. Song, Synthesis of FeOOH/Al_2O_3 composites with excellent adsorption performance and regenerability for phosphate removal from wastewater, Molecules 30 (21) (2025) 4200.

[38] L.H. Grey, H.Y. Nie, M.C. Biesinger, Defining the nature of adventitious carbon and improving its merit as a charge correction reference for XPS, Appl. Surf. Sci. 653 (2024) 159319.

[39] L.Å. Näslund, I. Persson, XPS spectra curve fittings of $Ti_3C_2T_x$ based on first principles thinking, Appl. Surf. Sci. 593 (2022) 153442.

[40] G. Beamson, High relution xps of organic polymers. the scienta esca 300 database, ICIplc (1992).

[41] S.K. Hazra, N.K. Kim, J. Park, B. Choi, S. Lee, T.Y. Choi, Gettering by cf4-ar plasma-treated titanium within anodically bonded glass-silicon microcavities, Sens. Mater. 21 (2009) 37–51.

[42] https://xpsdatabase.com/flfluorine-sspectra-tif4-tititanium-tetra-flfluoride/#Six-BE-Tables.

[43] M. Benchakar, L. Loupias, C. Garnero, T. Bilyk, C. Morais, C. Canaff, N. Guignard, S. Morisset, H. Pazniak, S. Hurand, P. Chartier, One MAX phase, different MXenes: a guideline to understand the crucial role of etching conditions on $Ti_3C_2T_x$ surface chemistry, Appl. Surf. Sci. 530 (2020) 147209.

[44] W. Luo, C. Jiang, Y. Li, S.A. Shevlin, X. Han, K. Qiu, Y. Cheng, Z. Guo, W. Huang, J. Tang, Highly crystallized α-FeOOH for a stable and efficient oxygen evolution reaction, J. Mater. Chem. A 5 (5) (2017) 2021–2028.

[45] C.Z. Wen, Q.H. Hu, Y.N. Guo, X.Q. Gong, S.Z. Qiao, H.G. Yang, From titanium oxydifluoride ($TiOF_2$) to titania (TiO_2): phase transition and non-metal doping with enhanced photocatalytic hydrogen (H 2) evolution properties, Chem. Commun. 47 (21) (2011) 6138–6140.

[46] J.Y. Ruzicka, F.A. Bakar, L. Thomsen, B.C. Cowie, C.M. Nicoll, T. Kemmitt, H.E. A. Brand, B. Ingham, G.G. Andersson, V.B. Golovko, XPS and NEXAFS study of fluorine modified TiO_2 nano-ovoids reveals dependence of Ti^{3+} surface population on the modifying agent, RSC Adv. 4 (2014) 20649–20658.

[47] A.N. Mansour, R.A. Brizzolara, Characterization of the surface of α-FeOOH powder by XPS, Surf. Sci. Spectra 4 (4) (1996) 357–362.

[48] Y.A. Teterin, S.N. Kalmykov, A.P. Novikov, Y.A. Sapozhnikov, L.D. Vukcevic, A. Y. Teterin, K.I. Maslakov, I.O. Utkin, A.B. Khasanova, N.S. Shcherbina, An XPS study of interaction of neptunyl (V) in aqueous solution with goethite (α-FeOOH), Radiochemistry 46 (6) (2004) 545–551.

[49] M. Golshan, N. Tian, G. Mamba, B. Kakavandi, Synergetic photocatalytic peroxymonosulfate oxidation of benzotriazole by copper ferrite spinel: factors and mechanism analysis, Toxics 11 (5) (2023) 429.

[50] Na Tian, Stefanos Giannakis, Leila Akbarzadeh, Farzad Hasanvandian, Emad Dehghanifard, Babak Kakavandi, Improved catalytic performance of ZnO via coupling with $CoFe_2O_4$ and carbon nanotubes: a new, photocatalysis-mediated peroxymonosulfate activation system, applied towards Cefixime degradation, J. Environ. Manag. 329 (2023) 117022.

[51] Y. Ma, Y. Duan, H. Su, Y. Li, Z. Chen, J. Li, Status and challenges of photocatalysis in environmental applications: Photocatalyst deactivation, Nano Res 18 (9) (2025) 94907750.

[52] W. Li, D. Shu, F. An, R. Liu, J. Shan, B. Han, S. Cao, Synchronization of Ti3C2 MXene/Fe^{3+} with sodium persulfate for the degradation of reactive dyes, npj Clean. Water 7 (1) (2024) 34.

[53] H.M. Abdelmigid, A.A. Alyamani, N.A. Hussien, M.M. Morsi, A. Alhumaidi, Integrated approaches for adsorption and incorporation testing of green-synthesized TiO_2 NPs mediated by seed-priming technology in Punica granatum L, Agronomy 12 (7) (2022) 1601.

[54] J. Rodríguez-Chueca, E. Alonso, D.N. Singh, Photocatalytic mechanisms for peroxymonosulfate activation through the removal of methylene blue: a case study, Inter. Int. J. Environ. Res. Public Health 16 (2) (2019) 198.

[55] R.M. Silverstein, G.C. Bassler, Spectrometric identification of organic compounds, J. Chem. Edu. 39 (11) (1962) 546.

[56] T. Parker, D. Zhang, D. Bugallo, K. Shevchuk, M. Downes, G. Valurouthu, A. Inman, B. Chacon, T. Zhang, C.E. Shuck, Y.J. Hu, Fourier-transform infrared spectral library of MXenes, Chem. Mater. 36 (17) (2024) 8437–8446.

[57] M. Žic, M. Ristić, S. Musić, Monitoring the hydrothermal precipitation of α-Fe_2O_3 from concentrated Fe $(NO_3)_3$ solutions partially neutralized with NaOH, J. Mol. Struct. 993 (1-3) (2011) 115–119.

[58] H. Deng, X. Li, Q. Peng, X. Wang, J. Chen, Y. Li, Monodisperse magnetic single-crystal ferrite microspheres, Angew. Chem. 117 (18) (2005) 2842–2845.

[59] H. Dai, W. Zhou, W. Wang, Co/N co-doped carbonaceous polyhedron as efficient peroxymonosulfate activator for degradation of organic pollutants: role of cobalt, Chem. Eng. J. 417 (2021) 127921.

[60] S. Atri, E. Loni, Z. Dyrcikova, F. Zazimal, M. Caplovicova, D. Dvoranova, G. Plesch, M. Kabatova, M. Brigante, M. Naguib, O. Monfort, Tailored MXene-derived nano-heterostructure oxides for peroxymonosulfate activation in the treatment of municipal wastewaters, Nanoscale 16 (39) (2024) 18430–18443.

[61] Z. Barbieriková, D. Dvoranová, V. Brezová, Application of EPR techniques in the study of photocatalytic systems. Materials Science in Photocatalysis, Elsevier, 2021, pp. 125–138.

[62] Y. Guo, L. Yan, X. Li, T. Yan, W. Song, T. Hou, C. Tong, J. Mu, M. Xu, Goethite/biochar-activated peroxymonosulfate enhances tetracycline degradation: Inherent roles of radical and non-radical processes, Sci. Total Environ. 783 (2021) 147102.

[63] H. Zhou, J. Peng, J. Li, J. You, L. Lai, R. Liu, Z. Ao, G. Yao, B. Lai, Metal-free black-red phosphorus as an efficient heterogeneous reductant to boost Fe^{3+}/Fe^{2+} cycle for peroxymonosulfate activation, Water Res. 188 (2021) 116529.

[64] Z. Sun, R. Zhu, T. Ding, X. Zhang, C. Li, Induced morphology orientation of α-FeOOH by kaolinite for enhancing peroxymonosulfate activation, J. Colloid Interface Sci. 626 (2022) 494–505.

[65] J. Ding, L. Shen, R. Yan, S. Lu, Y. Zhang, X. Zhang, H. Zhang, Heterogeneously activation of H_2O_2 and persulfate with goethite for bisphenol A degradation: a mechanistic study, Chemosphere 261 (2020) 127715.

[66] Y. Han, Z. Li, M. Zhang, F. Han, Z. Liu, W. Zhou, Isomorphic substitution of goethite by cobalt: effects on the pathway and performance of peroxymonosulfate activation, Chem. Eng. J. 450 (2022) 138460.

[67] D. Yu, L. Xu, K. Fu, X. Liu, S. Wang, M. Wu, W. Lu, C. Lv, J. Luo, Electronic structure modulation of iron sites with fluorine coordination enables ultra-effective H_2O_2 activation, Nat. Commun. 15 (1) (2024) 2241.

[68] B. Li, L.M. Sun, A. Li, C. Liu, Z.H. He, Y.J. Zhang, Y.X. Huang, X. Zhang, Utilizing MXene-mediated electron transfer pathway to boost peroxymonosulfate activation for water purification, Sep. Purif. Technol. 356 (2025) 129904.

[69] J. Liu, Z. Yao, G. Qiu, Y. Wan, W. Song, H. Zeng, F. Yang, D. Zhao, W. Yuan, P. Ju, R. Lin, Generation of reactive oxygen species through dissolved oxygen activation on defected porous carbon for efficient degradation of antibiotics, Chem. Eng. J. 455 (2023) 140602.

[70] T.D.D. Oliveira, W.S. Martini, M.D. Santos, M.A.C. Matos, L.L.D. Rocha, Caffeine oxidation in water by Fenton and Fenton-like processes: effects of inorganic anions and ecotoxicological evaluation on aquatic organisms, J. Braz. Chem. Soc. 26 (2015) 178–184.

[71] A. Nawaz, M. Molnárová, V.V. Kusumkar, M. Galamboš, S. Atri, O. Monfort, A. Fargašová, Toxicity assessment of MXene in Scenedesmus quadricauda physicochemical parameters, Water Air Soil Pollut. 236 (11) (2025) 750.